


 Cite this: *RSC Adv.*, 2022, **12**, 28451

Electronic, magnetic, optical and thermoelectric properties of co-doped $\text{Sn}_{1-2x}\text{Mn}_x\text{A}_x\text{O}_2$ ($\text{A} = \text{Mo, Tc}$): a first principles insight

 S. Laghzaoui, ^a A. Fakhim Lamrani, ^{ab} R. Ahl Laamara, ^{ac} E. Maskar, ^{*a} Botir Qonishevich Tuxtamishev, ^d Amel Laref ^e and D. P. Rai ^f

The electronic, magnetic, optical and thermoelectric (TE) properties of $\text{Sn}_{1-2x}\text{Mn}_x\text{A}_x\text{O}_2$ ($\text{A} = \text{Mo/Tc}$) have been examined using density functional theory (DFT) based on the FP-LAPW approach. The results suggested that all the doped compounds show a half-metallic ferromagnet property with a 100% spin polarization at the Fermi level within GGA and mBJ. Moreover, doping SnO_2 with double impurities reduces the bandgap. The reduced bandgaps are the result of impurity states which arise due to the Mn and Mo/Tc doping, leading to the shifts of the minima of the conduction band towards the Fermi energy caused by substantial hybridization between transition metals 3d–4d and O-2p states. Also, the (Mn, Mo) co-doped SnO_2 system exhibits a ferromagnetic ground state which may be explained by the Zener double exchange mechanism. While the mechanism that controls the ferromagnetism in the (Mn, Tc) co-doped SnO_2 system is p–d hybridization. Therefore, the role of this study is to illustrate the fact that half-metallic ferromagnet material is a good absorber of sunlight (visible range) and couples to give a combined effect of spintronics with optronics. Our analysis shows that $\text{Sn}_{1-2x}\text{Mn}_x\text{Mo}_x\text{O}_2$ and $\text{Sn}_{1-2x}\text{Mn}_x\text{Tc}_x\text{O}_2$ are more capable of absorbing sunlight in the visible range compared to pristine SnO_2 . In addition, we report a significant result for the thermoelectric efficiency ZT of ~ 0.114 and ~ 0.11 for $\text{Sn}_{1-2x}\text{Mn}_x\text{Mo}_x\text{O}_2$ and $\text{Sn}_{1-2x}\text{Mn}_x\text{Tc}_x\text{O}_2$, respectively. Thus, the coupling of these magnetic, optical, and thermoelectric properties in (Mn, A = Mo or Tc) co-doped SnO_2 can predict that these materials are suitable for optoelectronic and thermoelectric systems.

 Received 20th July 2022
 Accepted 12th September 2022

DOI: 10.1039/d2ra04499d

rsc.li/rsc-advances

1 Introduction

Transparent conducting oxides (TCOs) are materials that exhibit good optical transparency in the visible range, high electrical conductivity, and good carrier density.^{1,2} For photovoltaic conversion, a few micrometers thick film made of direct bandgap materials like II–VI or III–V compound semiconductors is sufficient.³ One of these materials, tin oxide (SnO_2), is characterized as having a large direct bandgap (3.6 eV)

at room temperature.^{4,5} SnO_2 currently occupies a prominent place because of the wide availability of the raw material and its non-toxicity. It is a semiconductor material possessing interesting physical properties which place it among the most promising in various fields such as optoelectronic devices, and solar cells and could be a good thermoelectric material.^{2,6} Interestingly, doping SnO_2 with transition metal elements (Mo, Cr, Mn, Rh, Co, Al, and Fe) induces a spin functionality which creates an opportunity in the field of electron spin that is being widely investigated today.^{7–11} This kind of material creates a new class of materials called diluted magnetic semiconductors (DMSSs).¹² Ferromagnetic behaviour has been reported in co-doped SnO_2 with a large magnetic moment of $\sim 7.0 \mu_{\text{B}}$ at room temperature.^{13,14} Ogale *et al.* reported that 5% Co doped SnO_2 is a high-temperature ferromagnet with $T_c = 650$ K and a giant magnetic moment.⁹ Also, Okabayashi *et al.*¹⁵ researched the ferromagnetic (FM) properties of samples and revealed that (Fe, Mn) co-doped SnO_2 preserves ferromagnetism. This study provides ample data on high optical absorption in the visible range and high electrical conductivity accomplished by impurity doping. Lin *et al.*,¹⁶ reported the effects of (Mn, Co) co-doped SnO_2 on optical characteristics. Their results show that the absorption efficiency of (Mn, Co) co-doped SnO_2 in visible light

^aLPHE-Modeling and Simulation, Faculty of Sciences, Mohammed V University in Rabat, Rabat, Morocco. E-mail: salma_laghzaoui@um5.ac.ma; maskar.fstmeca@gmail.com

^bENS-Rabat Physics Department, Mohammed V University in Rabat, B. P. 5118, Morocco. E-mail: fakhim@ens.um5.ac.ma

^cCentre of Physics and Mathematics (CPM), Faculty of Sciences, Mohammed V University in Rabat, Rabat, Morocco. E-mail: r.ahllaamara@um5r.ac.ma

^dCandidate of Technical Sciences, Vice Rector for Academic Affairs, Jizzakh State Pedagogical Institute, Uzbekistan

^eDepartment of Physics and Astronomy, College of Science, King Saud University, Riyadh, 11451, Saudi Arabia. E-mail: amel_la06@yahoo.fr

^fPhysical Sciences Research Center (PSRC), Department of Physics, Pachhunga University College, Mizoram University, Aizawl-796001, India. E-mail: dibya@pucollege.edu.in



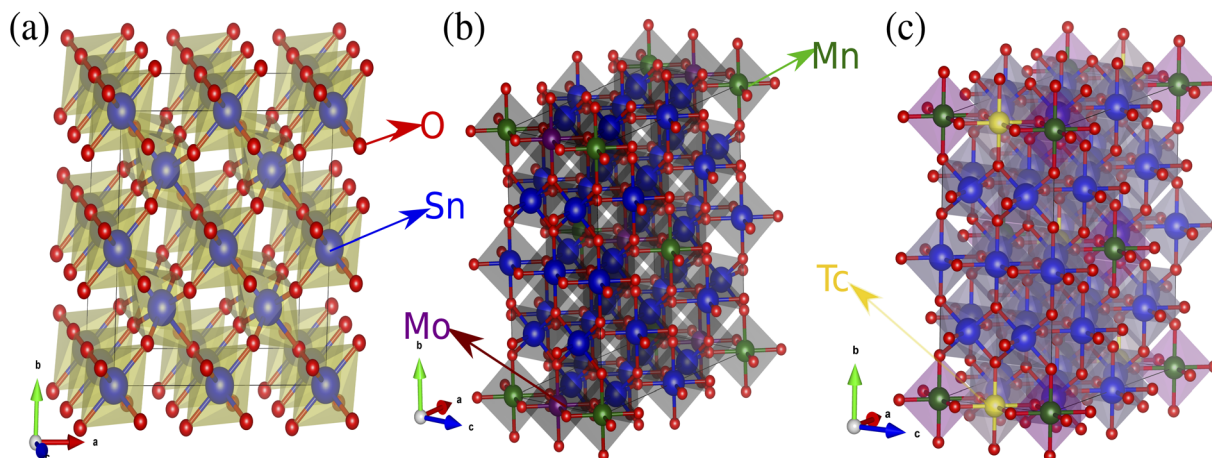


Fig. 1 $2 \times 2 \times 2$ supercell structures of (a) SnO_2 , (b) $\text{Sn}_{1-2x}\text{Mn}_x\text{MoxO}_2$ and (c) $\text{Sn}_{1-2x}\text{Mn}_x\text{TcxO}_2$.

was greatly improved. Spintronics coupled with optoelectronics has mostly remained an unexplored field despite the various research studies which have been carried out on this topic. A ferromagnetic DMS has yet to be used in the fabrication of solar cells, although it could be a vital material in future solar cell technology. SnO_2 co-doped with rare earth elements (Eu, Gd) demonstrates that this ferromagnetic alloy can absorb up to 96% in the visible light range and it can convert heat energy into electricity efficiently at room temperature.¹⁷ The efficiency of a thermoelectric material in converting heat into electrical energy is defined by the figure of merit, where S is the Seebeck coefficient, σ the electrical conductivity, K the total thermal conductivity and T the absolute temperature.^{18–26} The charge carrier concentration and mobility control both the Seebeck coefficient and the electrical conductivity. Additionally, some earlier studies showed that even magnetic materials give a significant good thermoelectric response, eventually improving the Seebeck coefficient such as: demonstration of magnon drag at relatively high temperatures,²⁷ paramagnon drag,^{28–30} spin fluctuation,³¹ spin entropy.³² Chang *et al.*³³ showed that doping $\text{RuSb}_{2+\delta}$ with Mn alters the electronic structure, creating a ferromagnetic (FM) conductor with good thermoelectric properties. Also, Yousuf *et al.* discovered the half-metallic ferromagnetic character of Zr_2NiZ ($Z = \text{Al, Ga}$) Heusler alloys, along with their effective thermoelectric coefficients, which points to the possibility of their use in the development of spintronic devices and impending thermoelectric materials.³⁴ The purpose of this work is to understand the properties of this ferromagnetic DMS under sunlight, particularly in the visible region, and how it might contribute to photovoltaic applications in a solar cell. As a result, we have examined the electronic, magnetic, optical, and thermoelectric properties of SnO_2 rutile doped with double impurities (Mn, A = Mo/Tc) using spin-polarized first-principles simulations. We have employed density functional theory (DFT) to perform our calculations, using the generalized gradient approximation (GGA-PBE)^{35,36} and the Tran-Blaha modified Becke-Johnson exchange potential approximation (TB-mBJ)^{37,38} as

implemented in WIEN2K Code.^{39,40} The details of our computational strategy are described in Section 2 of this work. Section 3 includes our findings. Finally, Section 4 concludes the results.

2 Computational details

Tin dioxide adopts a rutile-type quadratic lattice with a space group $P4_2/mnm$. The parameters of the crystal lattice are as follows: $a = b = 4.74$ Å and $c = 3.18$ Å.⁴¹ The unit cell contains six atoms, four oxygen atoms and two tin atoms. Each tin atom is in the middle of a cage formed by a regular octahedron of six oxygen atoms, while each oxygen atom is surrounded by three tin atoms located at the vertices of an isosceles triangle. The oxygen is in position 4f given by $[u, u, 0], [1 - u, 1 - u, 0], [u + 1/2, 1/2 - u, 1/2], [1/2 - u, u + 1/2, 1/2]$ with $u = 0.306$. Tin occupies position 2a, $[0, 0, 0], [1/2, 1/2, 1/2]$. In this work, the total calculations are obtained from *ab initio* calculations based on density functional theory (DFT) adopted by the full-potential linearized augmented plane wave (FP-LAPW) method. The cut-off parameter is set to $R_{\text{MT}} \times K_{\text{max}} = 7.5$, where K_{max} is the most valuable of the reciprocal lattice vectors in the plane wave expansion and R_{MT} is the smallest atomic sphere radii of most atomic spheres. Here the MT radii are chosen to be $R = 1.76$ au. To insert the double-impurities a supercell of $(2 \times 2 \times 2)$ mesh was created [$\text{Sn}_{16}\text{O}_{32}$ supercell, see Fig. 1(a)]. We have utilized a self-consistent criterion of the total energy with an accuracy of 10^{-6} Ry and charge difference $\Delta Q = 10^{-6}$ between two successive iterations, considering the force equal to 0.1 mRy per au. An energy of -6.5 Ry is utilized to separate the core states from the valence states. We have used a grid of 8813 k points and 557 points ($\text{Sn}_{14}\text{MnAO}_{32}$ supercell, with A = Mn/Tc) in the first Brillouin zone.⁴² In the supercell, the co-doped systems are developed by replacing two Sn atoms by Mn and A (= Mo/Tc) atoms relating to concentration ratios of $x = 0.0625$ in $\text{Sn}_{1-2x}\text{Mn}_x\text{A}_x\text{O}_2$ [see Fig. 1(b and c)]. To determine the most stable magnetic state, both ferromagnetic (FM) and antiferromagnetic (AFM) states are determined. The total energy difference $\Delta E = E_{\text{AFM}} - E_{\text{FM}}$,⁴³ determines the stabilization of the magnetic



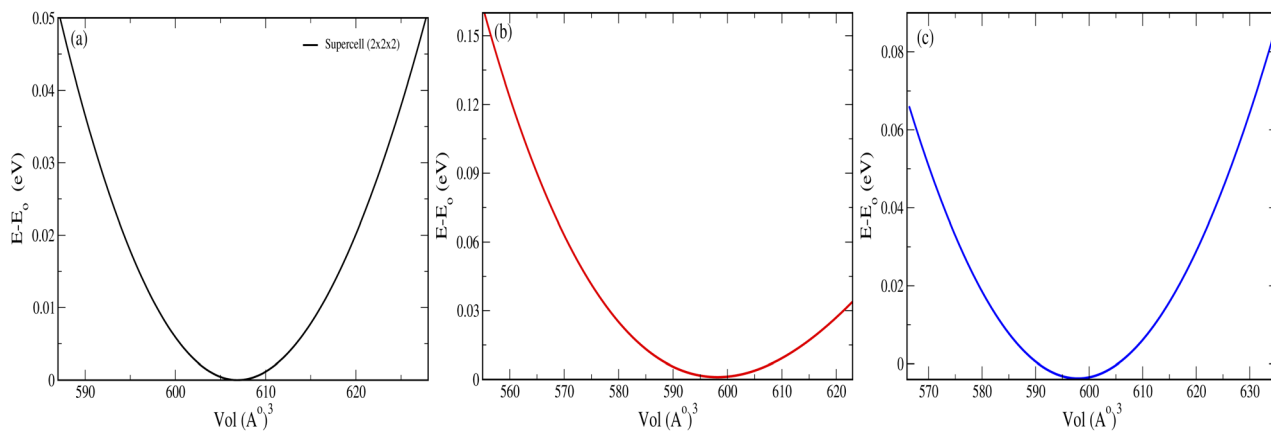


Fig. 2 Volume vs. energy curve of (a) SnO_2 ($2 \times 2 \times 2$), (b) $\text{Sn}_{1-2x}\text{Mn}_x\text{Mo}_x\text{O}_2$ and (c) $\text{Sn}_{1-2x}\text{Mn}_x\text{Tc}_x\text{O}_2$.

phase in the DMS. If the value is positive, the FM state is steady and stable but if the value is negative the AFM is steadily stable.

3 Results and discussion

3.1 Structural properties

The pristine and doped structures (SnO_2 , $\text{Sn}_{1-2x}\text{Mn}_x\text{Mo}_x\text{O}_2$ and $\text{Sn}_{1-2x}\text{Mn}_x\text{Tc}_x\text{O}_2$) were optimized by the volume optimization method. To obtain the most stable structure with minimum ground state energy, we performed the curve fitting of the energy-vs.-volume data within the Murnaghan equation of state⁴⁴ as:

$$E(V) = E_0 + \frac{9V_0B_0}{16} \left[\left[(V_0/V)^{2/3} - 1 \right]^3 B'_0 + \left[(V_0/V)^{2/3} - 1 \right]^2 \left[6 - 4(V_0/V)^{2/3} \right] \right] \quad (1)$$

where E_0 is the equilibrium energy, V_0 the original volume, V the obtained volume change, B is the bulk modulus and B' its first order pressure derivative. The smooth curves of energy-vs.-volume are obtained by fitting the data in the Murnaghan equation of state for the pristine and co-doped systems as shown in Fig. 2. The optimized lattice parameters are presented in Table 1 and are compared with the previous available data. For further analysis of structural stability of the doped and undoped materials we have calculated the formation energy (E_{for}) by using eqn (2):

$$E_{\text{for}} = E_{\text{tot}} - \sum_x E_x \quad (2)$$

where E_{tot} is the ground state total energy of the system, x is the number of individual components, E_x is the energy of an individual component in its bulk form. The calculated E_{for} for SnO_2 , $\text{Sn}_{1-2x}\text{Mn}_x\text{Mo}_x\text{O}_2$ and $\text{Sn}_{1-2x}\text{Mn}_x\text{Tc}_x\text{O}_2$ are -2.42 eV per atom, -1.57 eV per atom and -1.54 eV per atom, respectively. The negative values of E_{for} indicate the stability of our systems.

3.2 Electronic properties

As we are aware, the electronic properties are not properly described by GGA-PBE. Most of the time the GGA bandgaps are underestimated. Therefore, herein we have presented the electronic properties results by calculating the total and partial densities of states (DOS) of pure and co-doped SnO_2 by using the TB-mBJ potential. Firstly, we have studied the electronic structure of pristine SnO_2 in the absence of any doping elements. The total and partial densities of states of pristine SnO_2 are shown in Fig. 3 by using the TB-mBJ approximation. The electron state density displays perfect symmetry among

Table 1 Optimized lattice constant (\AA), bulk modulus (B) in GPa and its pressure derivative (B') for bulk SnO_2 and $\text{Sn}_{1-2x}\text{Mn}_x\text{A}_x\text{O}_2$ ($\text{A} = \text{Mo/Tc}$)

System	Lattice constant (our)		Bulk modulus B	Pressure derivative B'
	$a = b$	c		
$\text{Sn}_{1-2x}\text{Mn}_x\text{A}_x\text{O}_2$				
SnO_2	4.737	3.186	186.028	4.249
Ref. 7	4.767	3.129	—	—
Ref. 41	4.74	3.18	—	—
$\text{Sn}_{1-2x}\text{Mn}_x\text{Mo}_x\text{O}_2$	13.57	6.454	167.133	10.995
$\text{Sn}_{1-2x}\text{Mn}_x\text{Tc}_x\text{O}_2$	13.662	6.498	177.672	0.454

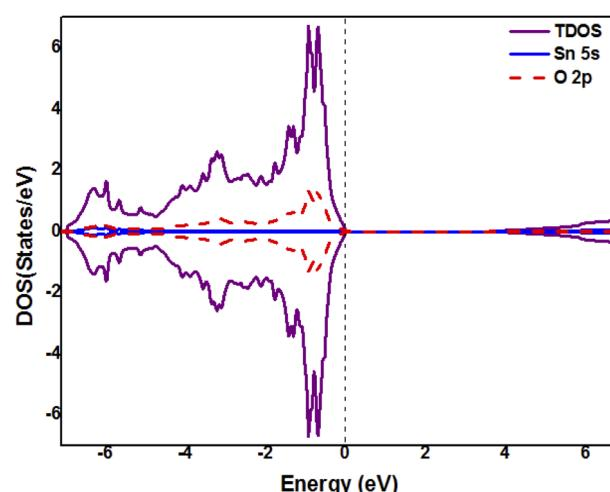


Fig. 3 Total and partial density of states (DOS) of pristine SnO_2 obtained from TB-mBJ.



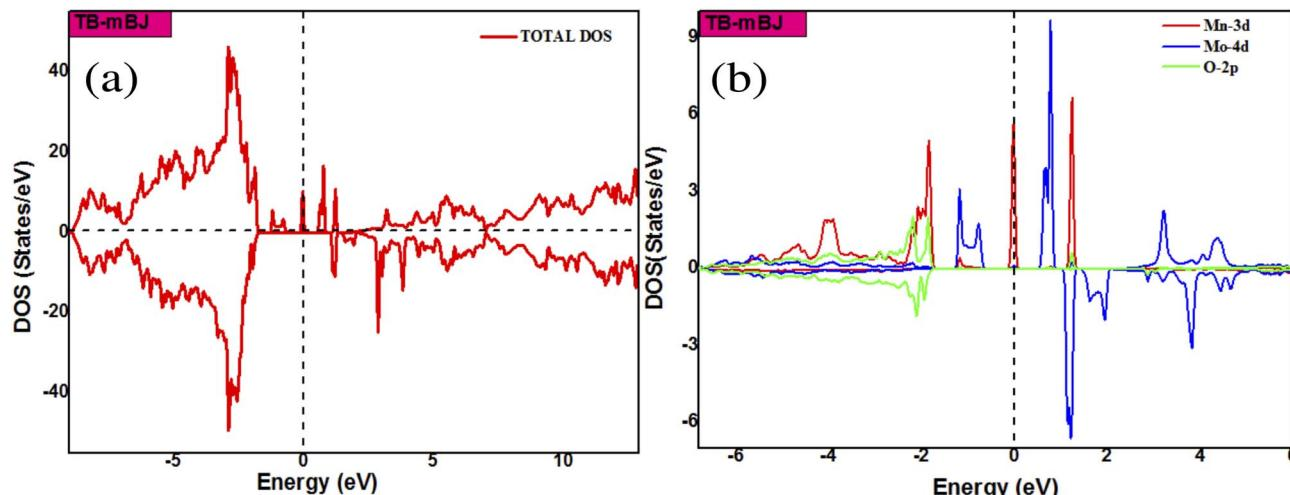


Fig. 4 The total (a) and partial (b) DOS of $\text{Sn}_{1-x}\text{Mn}_x\text{Mo}_x\text{O}_2$ using TB-mBJ approximation.

Table 2 The calculated results of the total energy E_{FM} , E_{AFM} , energy gap E_g , moment total m_{tot} and moment partial m_O , and m_{TM} for $\text{Sn}_{1-x}\text{Mn}_x\text{O}_2$, $\text{Sn}_{1-x}\text{Mo}_x\text{O}_2$, $\text{Sn}_{1-x}\text{Tc}_x\text{O}_2$, $\text{Sn}_{1-2x}\text{Mn}_x\text{Mo}_x\text{O}_2$ and $\text{Sn}_{1-2x}\text{Mn}_x\text{Tc}_x\text{O}_2$ obtained within the GGA-PBE/TB-mBJ approximation

Parameter	$\text{Sn}_{1-x}\text{Mn}_x\text{O}_2$	$\text{Sn}_{1-x}\text{Mo}_x\text{O}_2$	$\text{Sn}_{1-x}\text{Tc}_x\text{O}_2$	$\text{Sn}_{1-2x}\text{Mn}_x\text{Mo}_x\text{O}_2$	$\text{Sn}_{1-2x}\text{Mn}_x\text{Tc}_x\text{O}_2$
E_{FM} (Ry)	-40 596.428	-46 378.347	-46 852.367	-188 249.705	-188 723.737
E_{AFM} (Ry)	—	—	—	-188 249.704	-188 723.738
E_g (eV)	1.3	2.7	1.769	1.73/2.869	1.319/2.653
m_{tot} (μ_B)	3.0	2.0	3.0	5.0/5.0	6.0/6.003
m_{Mn} (μ_B)	2.87	—	—	3.51/3.71	2.97/3.025
m_{Mo} (μ_B)	—	1.31	—	0.81/0.79	—
m_{Tc} (μ_B)	—	—	1.87	—	1.82/2.091
m_O (μ_B)	-0.0023	-0.0097	0.0186	-0.0056/-0.0202	-0.005/-0.007

majority and minority spin states, which implies that SnO_2 is a non-magnetic material. The valence band is mainly formed by the O-2p orbitals and is full. While the conduction band is dominated by Sn-5s orbitals and is empty. The bandgaps calculated by using the TB-mBJ and GGA-PBE methods are 3.59 eV and 1.85 eV, respectively. In fact, the TB-mBJ approach gives a value for the bandgap closer to the experimental data.⁴⁵ Also, comparable results have been found in the previous theoretical calculations^{7,46,47} from PBE-GGA. The valence band has a width of 7.1 eV, which is in accordance with experimental and theoretical results.^{46,48}

To talk about the ferromagnetism in SnO_2 doped with dual impurities (Mn, A = Mo/Tc), we have calculated the electronic and magnetic properties of pure and co-doped SnO_2 corresponding to $x = 0.0625$ in the first step. Fig. 4(a and b) show the total and partial densities of states (DOS) calculated by using the TB-mBJ approach. We observed that the total DOS is asymmetrical, which is a signature of magnetic behaviour. The half-metallic character appears clear in these figures where the Fermi level crosses the majority spin band, while the spin-down band is empty. The presence of energy levels near the upper part of the bandgap facilitates the excitation of electrons to the conduction band. Therefore, these calculations predict 100% spin polarization at the Fermi level. The majority spin bands at

the Fermi level are mainly contributed by the Mo-d and Mn-d electrons, which suggests that the double impurities of Mn and Mo atoms do not result in the distortion of the nature of the host semiconductors.

The two possible magnetic configurations (FM and AFM) have been calculated and their energies compared. Our results indicate the stability of the ferromagnetic state in the $\text{Sn}_{1-2x}\text{Mn}_x\text{O}_2$ compound with a strong half-metallic behaviour. Further investigating the origin of ferromagnetism in the system, the electronic structure calculations indicate a sufficiently large magnetic moment of $5 \mu_B$ for the cell. The high value of the total magnetic moment indicates a strong interaction between the double impurities. Also, the Mn and Mo atoms assume a significant part in the generation of the total magnetic moment and the partial magnetic moments contributed by Mn and Mo are $3.51 \mu_B$ and $0.81 \mu_B$, respectively. These values are compared with those obtained in single doped $\text{Sn}_{1-x}\text{Mn}_x\text{O}_2$ ($m_{\text{Mn}} = 2.87 \mu_B$) and $\text{Sn}_{1-x}\text{Mo}_x\text{O}_2$ ($m_{\text{Mo}} = 1.31 \mu_B$). The value of m_{Mo} is in close agreement with our previous result $1.261 \mu_B$.⁷ The results for the total and partial magnetic moments are presented in Table 2. We could conclude that there is a charge transfer between the 4d electrons of the Mo atom and the 3d electrons of the Mn atom via the 2p orbitals of the O atom, to obtain an electronic configuration of d^3 on $[\text{Mn}^{3+} (3d^5)]$ and d^1



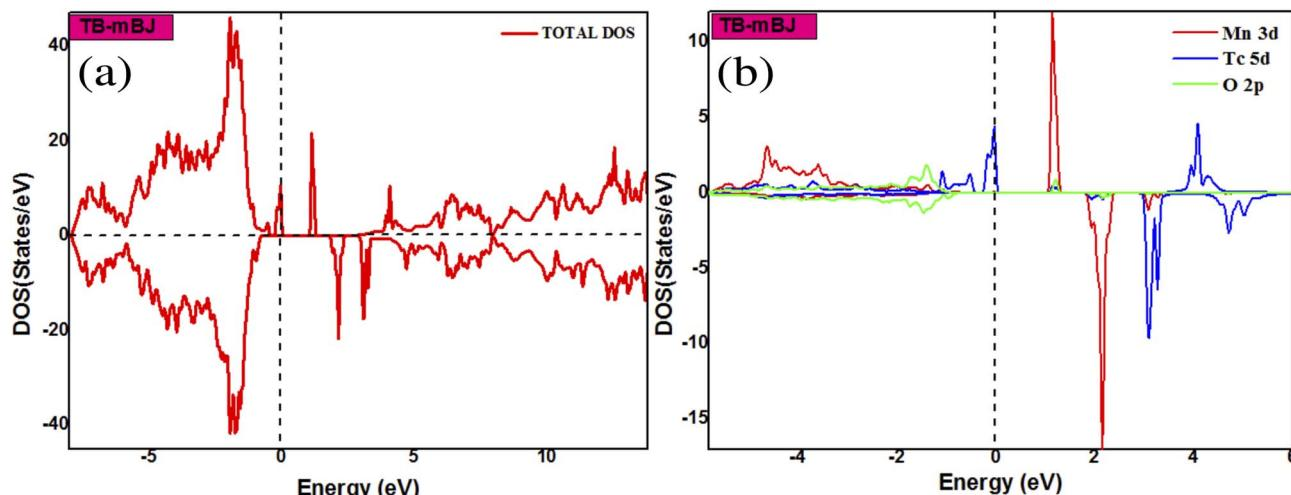


Fig. 5 The total (a) and partial (b) DOS of $\text{Sn}_{1-2x}\text{Mn}_x\text{Tc}_x\text{O}_2$ using TB-mBJ approximation.

on $[\text{Mo}^{5+} (5\text{d}^1)]$. In this manner, the mechanism responsible for ferromagnetic coupling is the Zener double exchange. As we have already discussed, the co-doping with Mn and Mo has brought about a drastic modification in the electronic and magnetic properties of SnO_2 . Furthermore, we have performed another co-doping by Mn and Tc with the concentration of $x = 0.0625$ by using TB-mBJ approximation. To inspect the stability of the magnetic phase in the (Mn, Tc) co-doped SnO_2 , we have calculated ΔE and we have found that the AFM state is more stable than the FM state. The total and partial densities of states of $\text{Sn}_{1-2x}\text{Mn}_x\text{Tc}_x\text{O}_2$ are shown in Fig. 5. Total DOS has significant asymmetry in the majority and minority spins, which comes from the Mn-3d, Tc-4d, and O-2p states. This suggests that the Mn-3d, Tc-4d and O-2p states have largely affected the induction of magnetic moment. Moreover, we could see that the spin-down state is empty, which is common in most of the DMS materials. The majority spin band shows 100% spin polarization at the Fermi level, bringing about the half-metallic behaviour. In addition, our calculation shows that the total magnetic moment is sufficiently large. The primary contribution to the total magnetic moment is from Mn ($m_{\text{Mn}} = 2.97 \mu_{\text{B}}$) and Tc ($m_{\text{Tc}} = 1.82 \mu_{\text{B}}$) atoms. Thus, we observe there is no exchange of charge between the Mn and Tc atoms. From Fig. 5, we have observed that the strong hybridization near the Fermi level is essentially brought about by Mn, Tc, and its neighbouring O atoms. Therefore, it is the p-d hybridization that is responsible for the magnetism in (Mn, Tc) co-doped SnO_2 . Consequently, the combination of all these characteristics in SnO_2 co-doped with (Mn, Tc), such as free flow of charge carriers and half-metallic behaviour with the high total magnetic moment, resulted in a quality of materials suitable for spintronic device fabrication. To confirm our *ab initio* findings, more experimentation will be required.

3.3 Optical properties

The optics of condensed media describe the interaction of an electromagnetic wave with the electrons of a solid. The linear

response of electromagnetic radiation is described utilizing the dielectric function as:

$$\varepsilon = \varepsilon_1 + i\varepsilon_2, \quad (3)$$

where $\varepsilon_1(\omega)$ and $\varepsilon_2(\omega)$ are the real and imaginary parts of the dielectric function. $\varepsilon_2(\omega)$ is inter-related to the electron transition between occupied and unoccupied states. The imaginary part defined the light absorption in the material and depends on the electronic transition; it is given by the following relation:⁴⁹

$$\varepsilon_2(\omega) = \frac{\hbar^2 e^2}{\pi m^2 \omega^2} \sum_{\vec{k}n' \vec{k}n} \left| \int d^3k \left| \langle \vec{k}n | \vec{p} | \vec{k}n' \rangle \right| \right|^2 [1 - f(\vec{k}n)] \delta(E_{\vec{k}n} - E_{\vec{k}n'} - \hbar\omega) \quad (4)$$

where \vec{p} is the momentum operator, $|\vec{k}n\rangle$ is the eigen-function of the eigenvalue, and $f(\vec{k}n)$ is the Fermi distribution function. The real part of the dielectric function $\varepsilon_1(\omega)$ is derived from the imaginary part $\varepsilon_2(\omega)$ using the Kramers-Kronig relation:⁵⁰

$$\varepsilon_1(\omega) = 1 + \frac{2}{\pi} \int_0^\infty \frac{\varepsilon_2(\omega') \omega' d\omega'}{\omega'^2 - \omega^2} \quad (5)$$

In this section, we investigate the effect of ferromagnetic behaviour based on transition metal (TM) co-doping SnO_2 on optical performance in natural light. The real part $\varepsilon_1(\omega)$ and the imaginary part $\varepsilon_2(\omega)$ of SnO_2 pure, (Mn, Mo) co-doped and (Mn, Tc) co-doped SnO_2 are shown in Fig. 6. We have considered the energy range of 0–12 eV. Table 3 lists the computed static dielectric constants using two approximations, GGA-PBE and TB-mBJ, which are raised with the TM added. At lower energies, the real part has a higher value, indicating that the polarization capacity is greater. $\varepsilon_1(\omega)$ shows negative values in the high energy region, as shown in Fig. 6(a and b), which means that most of the incident light is reflected due to the phenomenon of anomalous dispersion and the materials exhibit metallic



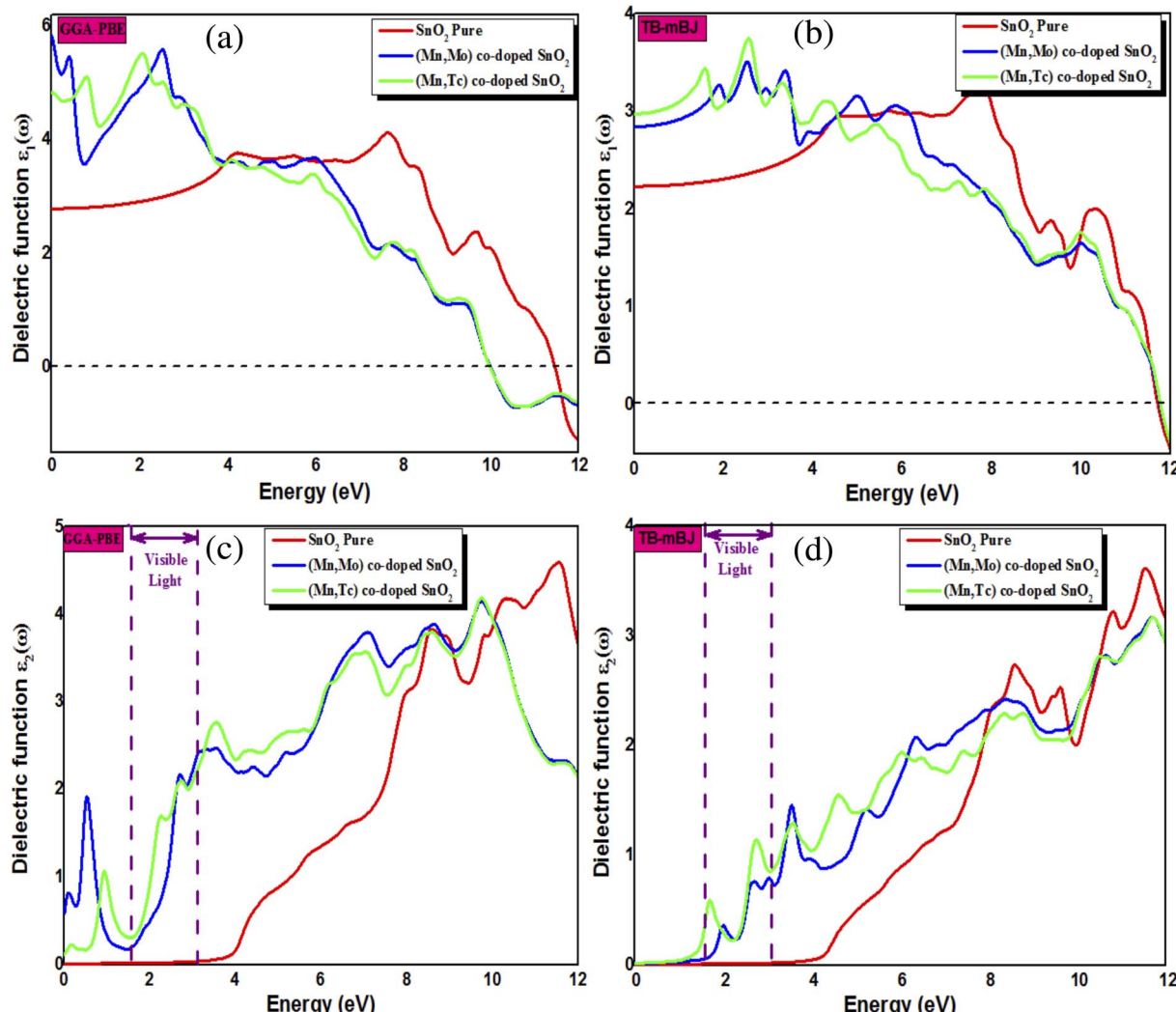


Fig. 6 The calculated $\varepsilon_1(\omega)$ (a, b) and $\varepsilon_2(\omega)$ (c, d) using GGA-PBE and TB-mBJ approximations.

Table 3 Optical properties of bulk SnO_2 and $\text{Sn}_{1-2x}\text{Mn}_x\text{A}_x\text{O}_2$ ($x = 0.0625$) at zero energy

System Parameter	GGA-PBE)			TB-mBJ		
	SnO_2	$\text{Sn}_{1-2x}\text{Mn}_x\text{Mo}_x\text{O}_2$	$\text{Sn}_{1-2x}\text{Mn}_x\text{Tc}_x\text{O}_2$	SnO_2	$\text{Sn}_{1-2x}\text{Mn}_x\text{Mo}_x\text{O}_2$	$\text{Sn}_{1-2x}\text{Mn}_x\text{Tc}_x\text{O}_2$
$\varepsilon_1(0)$	2.79	5.83	4.83	2.23	2.84	2.97
$n(0)$	1.67	2.41	2.19	1.49	1.68	1.72
$R(0)\%$	6.29	17.13	13.99	3.93	6.51	7.06

behaviour. We are interested in the imaginary part of the dielectric function in this study to assess the various transitions between the occupied states beneath the Fermi level and the unoccupied states higher than the Fermi level due to photon absorption. From Fig. 6(c and d), the curve of the imaginary part is zero in the low energy region for pure SnO_2 due to its high transmission in these regions. This is similar to the calculation performed for SnO_2 without doped elements.⁵¹⁻⁵³ Comparing with the (Mn, Mo) co-doped and (Mn, Tc) co-doped SnO_2 systems, we can find new peaks in the low energy region. These

peaks present interband transitions of the electrons between the top of the valence band and the bottom of the conduction band, which indicate the response of these systems to visible and IR light. The knowledge of the real part and the imaginary part of the dielectric function allows calculation of other optical parameters such as absorption coefficient $\alpha(\omega)$, refractive index $n(\omega)$, loss spectrum $L(\omega)$ and reflectivity $R(\omega)$.^{49,50}

$$\alpha(\omega) = \frac{2\omega(|\varepsilon(\omega)| - \text{Re}\varepsilon(\omega))^{1/2}}{c} \quad (6)$$

$$R(\omega) = \left| \frac{\sqrt{\varepsilon(\omega) - 1}}{\sqrt{\varepsilon(\omega) + 1}} \right|^2 \quad (7)$$

$$L(\omega) = \frac{\varepsilon_2(\omega)}{\varepsilon_1^2(\omega) + \varepsilon_2^2(\omega)} \quad (8)$$

$$n = \sqrt{\frac{1}{2} \left((\varepsilon_1^2 + \varepsilon_2^2)^{1/2} + \varepsilon_1 \right)} \quad (9)$$

where $\varepsilon(\omega) = \sqrt{\varepsilon_1^2(\omega) + \varepsilon_2^2(\omega)}$.

The absorption coefficient $\alpha(\omega)$ reflects a measure of the intensity of electromagnetic radiation as it crosses through any material. Fig. 7 shows the absorption coefficient spectra as a function of the photon energy of SnO_2 , (Mn, Mo) and (Mn, Tc) co-doped SnO_2 . The absorption coefficient curves for both (Mn, Mo) and (Mn, Tc) co-doped SnO_2 exhibit new peaks in the lower

energies compared to pure SnO_2 . So, we demonstrate that the introduction of TM brings the visible red-shift phenomenon. The high value of the absorption coefficient in the ultraviolet region contributes to an extremely efficient photon conversion process, which means that a quantum cut may be observed in the systems co-doped with transition metals.^{17,54,55} This result provides a new idea for developing and using SnO_2 -based optics.

The calculated refractive index $n(\omega)$, reflectivity $R(\omega)$ and loss spectrum $L(\omega)$ using the GGA-PBE and TB-mBJ approach depending on photon energy are displayed in Fig. 8, 9 and 10 for SnO_2 , $\text{Sn}_{1-2x}\text{Mn}_x\text{Mo}_x\text{O}_2$ and $\text{Sn}_{1-2x}\text{Mn}_x\text{Tc}_x\text{O}_2$ with $x = 0.0625$. Table 3 lists the calculated refractive indices at zero energy $n(0)$. We can see that these materials have a high refractive index in the infrared and visible regions, which drops at higher energy in the ultraviolet region. This reduction in value is because of the

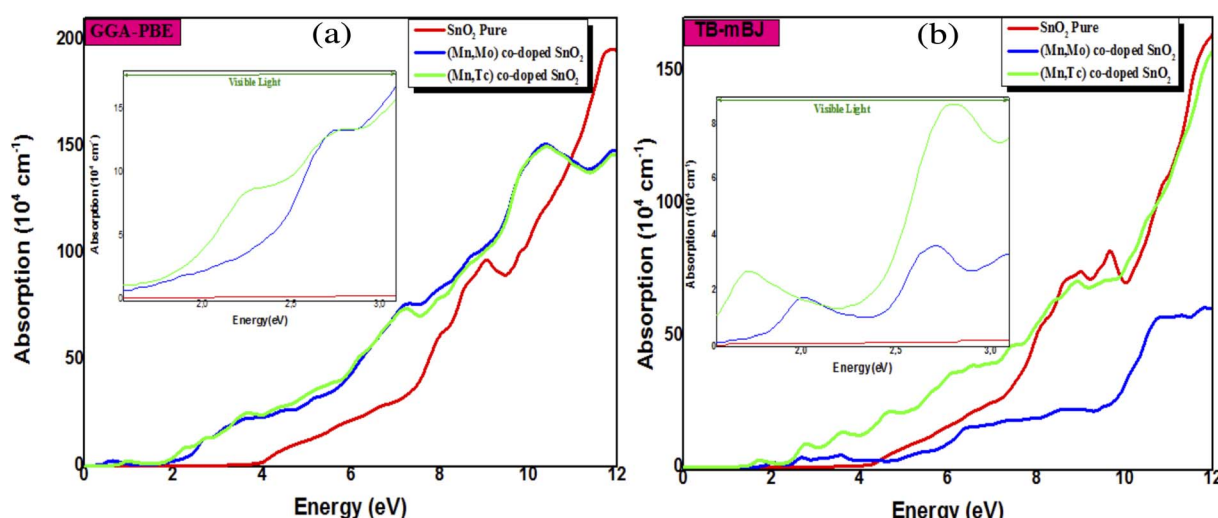


Fig. 7 Absorption spectra of SnO_2 pure, $\text{Sn}_{1-2x}\text{Mn}_x\text{Mo}_x\text{O}_2$ and $\text{Sn}_{1-2x}\text{Mn}_x\text{Tc}_x\text{O}_2$ ($x = 0.0625$) by using GGA-PBE (a) and TB-mBJ (b).

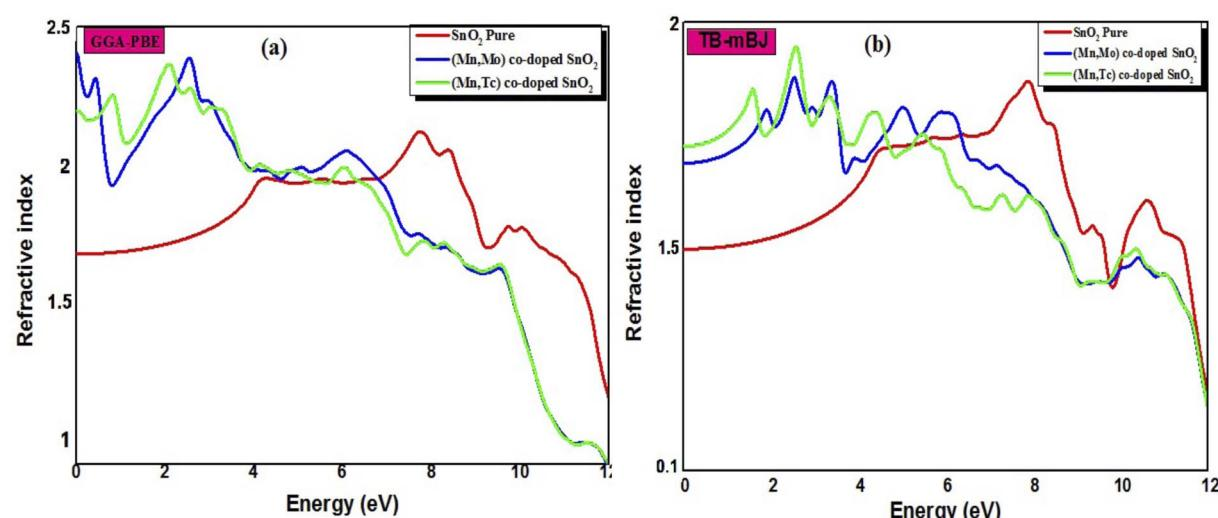


Fig. 8 The refractive index of SnO_2 pure, $\text{Sn}_{1-2x}\text{Mn}_x\text{Mo}_x\text{O}_2$ and $\text{Sn}_{1-2x}\text{Mn}_x\text{Tc}_x\text{O}_2$ ($x = 0.0625$) from (a) GGA-PBE and (b) TB-mBJ.

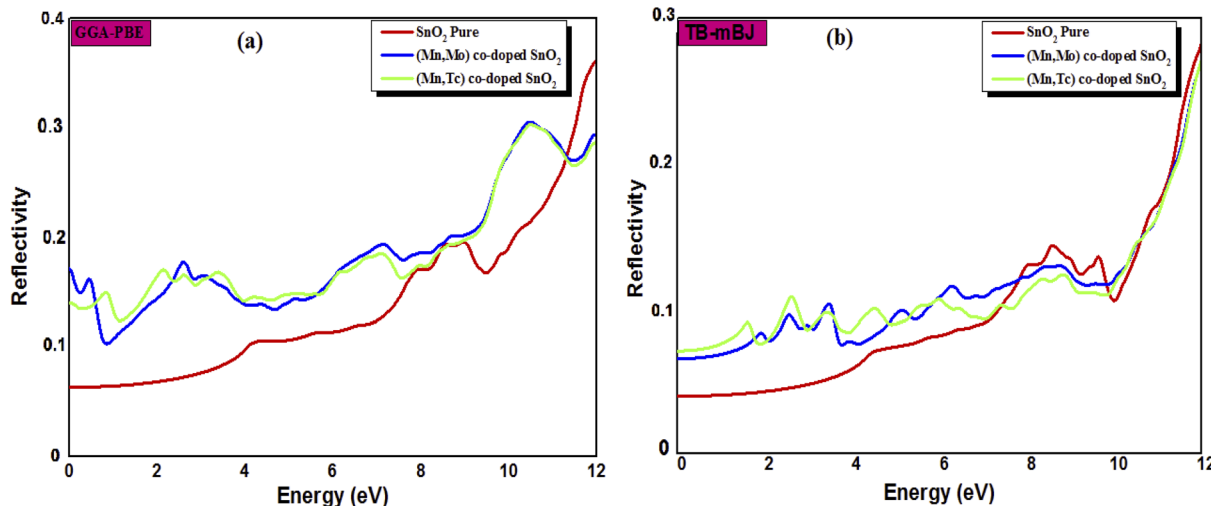


Fig. 9 The reflectivity index of SnO_2 pure, $\text{Sn}_{1-2x}\text{Mn}_x\text{Mo}_x\text{O}_2$ and $\text{Sn}_{1-2x}\text{Mn}_x\text{Tc}_x\text{O}_2$ ($x = 0.0625$) from (a) GGA-PBE and (b) TB-mBJ.

optical dispersion behaviour of the material. The reflectivity $R(0)$ is given in Table 3, which is less than 18% for all the compounds. The reflectivity increases as we get closer to the high energy zone, as shown in Fig. 9. This reflectivity result can enable these compounds to be used as a selective reflector in the UV region. The loss function describes the energy loss of electrons as they move through a material. The loss occurs when there is a transition between the valence and conduction band. Fig. 10 shows the energy loss function depending on photon energy using GGA-PBE and TB-mBJ approximations. The loss function curve increases gradually with an increase in photon energy. Moreover, the peaks of the electron energy loss $L(\omega)$ spectrum represent the information linked to the plasma resonance and the next frequency to which the electrons respond is recognized as the plasma frequency.⁵⁶ Thus, the half-metallic ferromagnet can improve the optical characteristics, such as absorption in visible light transferring electrons from

the valence band to the conduction band, which is required for greater photovoltaic conversion.

3.4 Thermoelectric properties

The thermoelectric effect contributes to the conversion of energy, which can be electrical energy generated from heat. A great thermoelectric material has a large value for the electrical conductivity (σ), which can limit the internal Joule heat loss, a high Seebeck coefficient (S) to deliver the greatest possible voltage, and a low thermal conductivity ($K = K_e + K_\lambda$) where K_e is the electronic thermal conductivity due to the charge carriers and K_λ represents the contribution due to the thermal vibrations of the network (phonons). To decouple the σ/τ and κ/τ , we have considered the constant relaxation time ($\tau = 10^{-14}$ s).^{57,58} These properties are executed in the BoltzTraP code, utilizing the Boltzmann semiclassical theory.⁵⁹ After that, the calculation

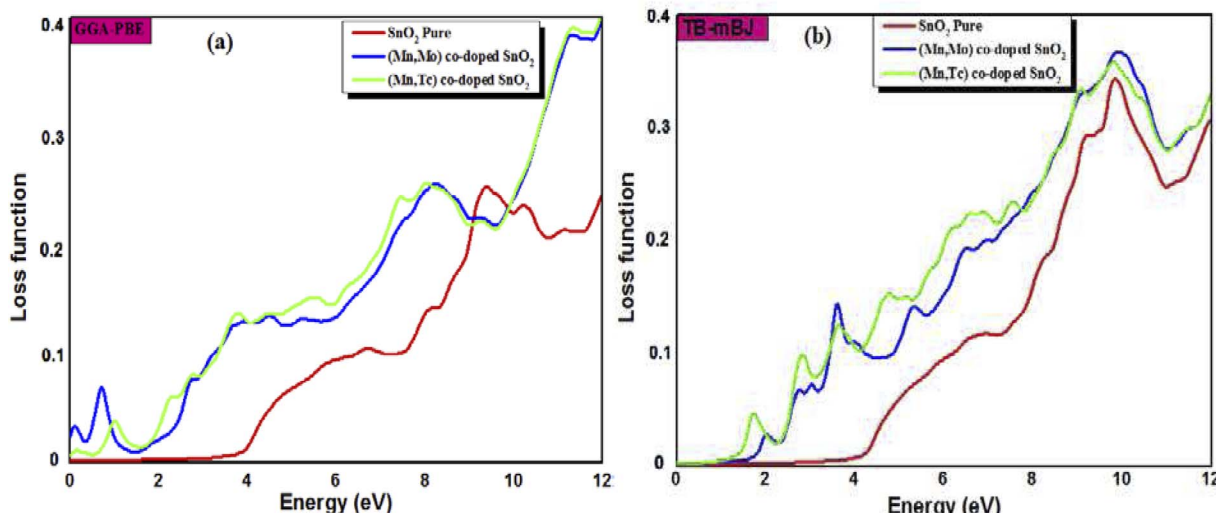


Fig. 10 The loss function spectra of SnO_2 pure, $\text{Sn}_{1-2x}\text{Mn}_x\text{Mo}_x\text{O}_2$ and $\text{Sn}_{1-2x}\text{Mn}_x\text{Tc}_x\text{O}_2$ ($x = 0.0625$) from (a) GGA-PBE and (b) TB-mBJ.



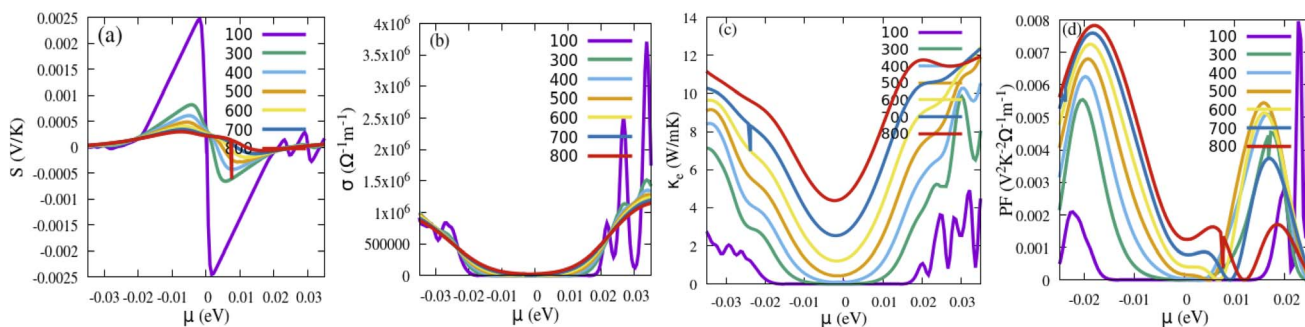


Fig. 11 (a) Seebeck coefficient, (b) electrical conductivity, (c) thermal conductivity and (d) power factor as a function of chemical potential for $\text{Sn}_{1-2x}\text{Mn}_x\text{Mo}_x\text{O}_2$.

is done by the GGA-mBJ approximation. The Seebeck coefficient depicts the ability to create an electric potential from a temperature gradient. From Fig. 11a and 12a, we can see that the positive S values are high, indicating the holes are the majority carriers and the dominant role of p-type behaviour for instigating a potential difference. The Seebeck coefficient (S) curves for both $\text{Sn}_{1-2x}\text{Mn}_x\text{Mo}_x\text{O}_2$ and $\text{Sn}_{1-2x}\text{Mn}_x\text{Tc}_x\text{O}_2$ compounds exhibit a decreasing trend with increasing temperature. The high Seebeck coefficient values of these materials at low temperatures, especially at room temperature, make them potential low-temperature thermoelectric materials. The electrical conductivity per relaxation (σ) as a function of chemical potential (μ) for each temperature is illustrated in Fig. 11b and 12b. We can see that the value of the electrical conductivity of (Mn, Mo/Tc) co-doped SnO_2 increases near the Fermi level as the temperature rises, owing to that more electrons can jump from the valence band to the conduction band. As a result, the energized electrons are changed over into charge carriers, which show increasing behaviour with temperature. At room temperature, the values of σ are $5.700 \times 10^5 \Omega^{-1} \text{ m}^{-1}$ and $1.700 \times 10^5 \Omega^{-1} \text{ m}^{-1}$ for $\text{Sn}_{1-2x}\text{Mn}_x\text{Mo}_x\text{O}_2$ and $\text{Sn}_{1-2x}\text{Mn}_x\text{Tc}_x\text{O}_2$ ($x = 0.0625$), respectively. However, the electron part of the thermal conductivity (K_e) for both $\text{Sn}_{1-2x}\text{Mn}_x\text{Mo}_x\text{O}_2$ and $\text{Sn}_{1-2x}\text{Mn}_x\text{Tc}_x\text{O}_2$ are presented in Fig. 11c and 12c. The K_e value increases with the increase in temperature for (Mn, Mo/Tc) co-doped SnO_2 . In this situation, the high temperatures improve the charge density through electronic vibrations. The crucial

factor for selecting the best fit materials for the thermoelectric component is offered by the power factor $\text{PF} = S^2\sigma$ [see Fig. 11d and 12d]. The room temperature values of PF for $\text{Sn}_{1-2x}\text{Mn}_x\text{Mo}_x\text{O}_2$ and $\text{Sn}_{1-2x}\text{Mn}_x\text{Tc}_x\text{O}_2$ are $54 \times 10^{-4} (\text{V}^2 \text{ K}^{-2} \Omega^{-1} \text{ m}^{-1})$ and $12 \times 10^{-4} (\text{V}^2 \text{ K}^{-2} \Omega^{-1} \text{ m}^{-1})$, respectively. A material's ability for heat energy conversion into electrical energy is given by the figure of merit, $ZT = \frac{S^2\sigma}{K_e + K_\lambda} T$. A ZT value of ~ 1 indicates the optimum with 30% applicability. The calculation of ZT is tricky and challenging due to the unavailability of a direct approach in calculating K_λ and also computationally is very expensive. However, we will use the technique to achieve the minimum K_λ value by considering the minimum phonon mean free path. The rough estimation of K_λ (minimum) is obtained from the bulk modulus and volume relation of the unit cell structure from DFT given by eqn (10):^{60,61}

$$K_\lambda(\text{min}) = 1.2 K_B M_{\text{av}}^{-1/2} B^{1/2} V^{-1/6} \quad (10)$$

where K_B is the Boltzmann constant, M_{av} is average atomic mass ($M_{\text{av}} = M/nN_A$), M is the molecular mass, N_A is Avogadro's number, n is number of atoms in the unit cell, B is the bulk modulus, and V is average atomic volume. The minimum K_λ values of $\text{Sn}_{1-2x}\text{Mn}_x\text{Mo}_x\text{O}_2$ and $\text{Sn}_{1-2x}\text{Mn}_x\text{Tc}_x\text{O}_2$ are 11.15 and $3.08 (\text{W m}^{-1} \text{ K}^{-1})$, respectively. Now considering these K_λ as the minimum and K_e values of $3.03 (\text{W m}^{-1} \text{ K}^{-1})$ and $1.21 (\text{W m}^{-1} \text{ K}^{-1})$, we could predict the $K_{\text{total}} = K_\lambda + K_e$ at 300 K , and consequently a rough estimation of ZT values at RT being 0.114 and

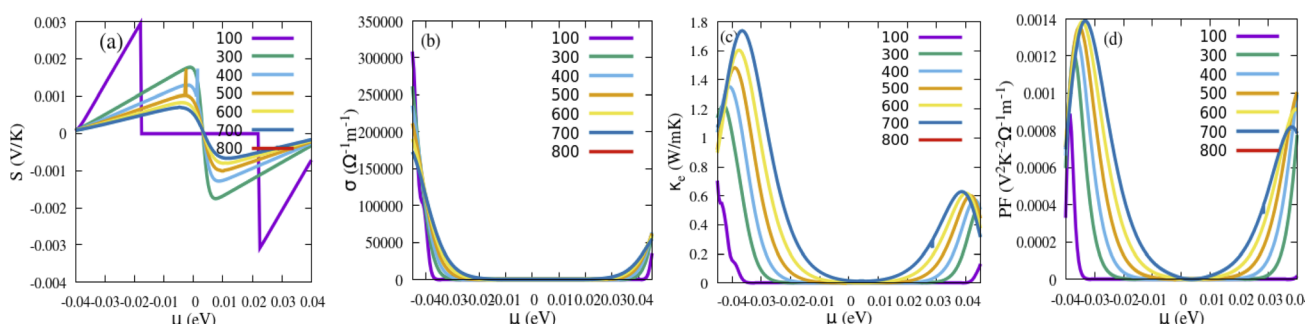


Fig. 12 (a) Seebeck coefficient, (b) electrical conductivity, (c) thermal conductivity and (d) power factor as a function of chemical potential for $\text{Sn}_{1-2x}\text{Mn}_x\text{Tc}_x\text{O}_2$.

0.11 for $\text{Sn}_{1-2x}\text{Mn}_x\text{Mo}_x\text{O}_2$ and $\text{Sn}_{1-2x}\text{Mn}_x\text{Te}_x\text{O}_2$, respectively. The results suggest that these materials give significant thermoelectric responses at low temperature, although the result is low as compared to the bench mark value of unity at high temperature. Indeed, the presence of all these traits in these ferromagnetic materials, such as the absorption of sunlight, and the ability to convert heat energy into electricity efficiently, indicates that these materials have a high potential for application in thermoelectric devices and could be crucial materials for the development of solar cells as well in the future.

4 Conclusions

In this work, we investigated the electronic, magneto-optical, and thermoelectric properties of $\text{Sn}_{1-2x}\text{Mn}_x\text{Mo}_x\text{O}_2$ and $\text{Sn}_{1-2x}\text{Mn}_x\text{Te}_x\text{O}_2$ ($x = 0.0625$) based on a first principles study using two approximations, GGA-PBE and TB-mBJ. The findings demonstrate that SnO_2 doping with double impurities improved the magnetism in the materials so that the half-metallic behaviour was found with 100% polarization at the Fermi level. The mechanisms that control the ferromagnetism in these compounds $\text{Sn}_{1-2x}\text{Mn}_x\text{Mo}_x\text{O}_2$ and $\text{Sn}_{1-2x}\text{Mn}_x\text{Te}_x\text{O}_2$ are the double Zener exchange and the p-d exchange mechanisms, respectively. The results further show that these materials $\text{Sn}_{1-2x}\text{Mn}_x\text{A}_x\text{O}_2$ ($\text{A} = \text{Mo/Tc}$) can improve the absorption of sunlight in low energy regions compared to pristine SnO_2 and have good thermoelectric properties. Thus, the coupling of these magnetic, optical, and thermoelectric properties in ($\text{Mn, A} = \text{Mo or Tc}$) co-doped SnO_2 systems can predict that these materials are suitable for better efficacy photovoltaic transformation in solar cells.

Conflicts of interest

There are no conflicts to declare.

Acknowledgements

The author (A. Laref) acknowledges support from the "Research Center of the Female Scientific and Medical Colleges", Deanship of Scientific Research, King Saud University.

References

- 1 K. Subramanyam, N. Sreelekha, G. Murali, D. Amaranatha Reddy and R. P. Vijayalakshmi, Structural, optical and magnetic properties of Cr doped SnO_2 nanoparticles stabilized with polyethylene glycol, *Phys. B*, 2014, **454**, 86–92.
- 2 S. A. Wolf, D. D. Awschalom, R. A. Buhrman, J. M. Daughton, S. V. Molnar, M. L. Roukes, A. Y. Chtchelkanova and D. M. Treger, Spintronics: a spin-based electronics vision for the future, *Science*, 2001, **294**, 1488–1495.
- 3 P. K. Tawalare, Optimizing photovoltaic conversion of solar energy, *AIP Adv.*, 2021, **11**, 100701.
- 4 M. Batzill, K. Katsiev and U. Diebold, Surface morphologies of SnO_2 (110), *Surf. Sci.*, 2003, **529**, 295–311.
- 5 V. P. Senthil Srinivasan, M. K. Patra, V. S. Choudhary, M. Mathew and A. Pandya, Phase-change annealing effects on electrical and optical properties of tin oxide thin films, *J. Optoelectron. Adv. Mater.*, 2010, **12**(7), 1485–1489.
- 6 M. Hammi, O. El Rhazouani, M. Arejdal and A. Slassi, Ab initio study of semi-classic transport coefficients of SnO_2 thermoelectric material, *Chin. J. Phys.*, 2017, **55**, 187–194.
- 7 D. P. Rai, A. Laref, A. Shankar, A. P. Sakhya, R. Khenata and R. K. Thapa, Spin-induced transition metal (TM) doped SnO_2 a dilute magnetic semiconductor (DMS): A first principles study, *J. Phys. Chem. Solids*, 2018, **120**, 104–108.
- 8 N. H. Hong, J. Sakai, W. Prellier and A. Hassini, Transparent Cr-doped SnO_2 thin films: ferromagnetism beyond room temperature with a giant magnetic moment, *J. Phys.: Condens. Matter*, 2005, **17**(10), 1697.
- 9 S. B. Ogale, R. J. Choudhary, J. P. Buban, S. E. Lofland, S. R. Shinde, S. N. Kale, V. N. Kulkarni, J. Higgins, C. Lanci, J. R. Simpson, N. D. Browning, S. D. Sarma, H. D. Drew, R. L. Greene and T. Venkatesan, High temperature ferromagnetism with a giant magnetic moment in transparent Co-doped $\text{SnO}_{2-\delta}$, *Phys. Rev. Lett.*, 2003, **91**, 077205.
- 10 J. Wang, D. Zhou, Y. Li and P. Wu, Experimental and first-principle studies of ferromagnetism in Na-doped SnO_2 nanoparticles, *Vacuum*, 2017, **141**, 62–67.
- 11 N. Kumari, A. Ghosh, S. Tewari and A. Bhattacharjee, Synthesis, structural and optical properties of Al doped SnO_2 nanoparticles, *Indian J. Phys.*, 2014, **88**, 65–70.
- 12 T. Fukumura, Y. Yamada, H. Toyosaki, T. Hasegawa, H. Koinuma and M. Kawasaki, Exploration of oxide-based diluted magnetic semiconductors toward transparent spintronic, *Appl. Surf. Sci.*, 2004, **223**, 62–67.
- 13 A. Punnoose and J. Hays, Possible metamagnetic origin of ferromagnetism in transition-metal doped SnO_2 , *J. Appl. Phys.*, 2005, **97**, 10D321.
- 14 N. Nomura, J. Okabayashi, K. Okamura and Y. Yamada, Magnetic properties of Fe and Co codoped SnO_2 prepared by sol-gel method, *J. Appl. Phys.*, 2011, **110**, 083901.
- 15 J. Okabayashi, K. Nomura, S. Kono and Y. Yamada, Magnetization enhancement in room-temperature ferromagnetic Fe-Mn co-doped SnO_2 , *Jpn. J. Appl. Phys.*, 2012, **51**, 023003.
- 16 L. Lin, R. Chen, C. He, H. Tao, J. Huang, L. Zhu, L. Yan and J. Zhang, Magnetic and optical properties of (Mn, Co) co-doped SnO_2 , *Vacuum*, 2020, **182**, 109681.
- 17 A. F. Lamrani, Ferromagnetic alloy for high-efficiency photovoltaic conversion in solar cells: first-principles insights when doping SnO_2 rutile with coupled Eu-Gd, *RSC Adv.*, 2021, **11**, 7096–7106.
- 18 P. Ruleova, C. Drasar, P. Lostak, C. P. Li, S. C. Ballikaya and C. Uher, Thermoelectric properties of $\text{Bi}_2\text{O}_2\text{Se}$, *Mater. Chem. Phys.*, 2010, **119**, 299–302.
- 19 X. Qu, W. Wang, W. Liu, Z. Yang, X. Duan and D. Jia, Antioxidation and Thermoelectric properties of ZnO nanoparticles-coated $\beta\text{-FeSi}_2$, *Mater. Chem. Phys.*, 2011, **129**, 331–336.



20 Q. Hao, D. Xu and H. Zhao, Computation-Driven Materials Search for Thermoelectric Application, *ECS J. Solid State Sci. Technol.*, 2017, **6**(3), N3095–N3102.

21 F. J. Disalvo, Thermoelectric Cooling and Power Generation, *Science*, 1999, **285**, 703–706.

22 J. R. Sootsman, D. Y. Chung and M. G. Kanatzidis, New and old concepts in thermoelectric materials, *Angew. Chem., Int. Ed.*, 2009, **48**(46), 8616–8639.

23 T. Xing, Q. Song, P. Qiu, Q. Zhang, M. Gu, X. Xia, J. Liao, X. Shi and L. Chen, High efficiency GeTe-based materials and modules for thermoelectric power generation, *Energy Environ. Sci.*, 2021, **14**, 995.

24 Z. Liu, N. Sato, W. Gao, K. Yubuta, N. Kawamoto, M. Mitome, K. Kurashima, Y. Owada, K. Nagase, C. Lee, J. Yi, K. Tsuchiya and T. Mori, Demonstration of ultrahigh thermoelectric efficiency of ~7.3% in $Mg_3Sb_2/MgAgSb$ module for low-temperature energy harvesting, *Joule*, 2021, **5**, 1196–1208.

25 P. Ying, R. He, J. Mao, Q. Zhang, H. Reith, J. Sui, Z. Ren, K. Nielsch and G. Schierning, Towards tellurium-free thermoelectric modules for power generation from low-grade heat, *Nat. Commun.*, 2021, **12**, 1121.

26 F. Guo, B. Cui, C. Li, Y. Wang, J. Cao, X. Zhang, Z. Ren, W. Cai and J. Sui, Ultrahigh Thermoelectric Performance in Environmentally Friendly SnTe Achieved through Stress-Induced Lotus-Seedpod-Like Grain Boundaries, *Adv. Funct. Mater.*, 2021, **31**, 2101554.

27 R. Ang, A. U. Khan, N. Tsujii, K. Takai, R. Nakamura and T. Mori, Thermoelectricity Generation and Electron-Magnon Scattering in a Natural Chalcopyrite Mineral from a Deep-Sea Hydrothermal Vent, *Angew. Chem., Int. Ed.*, 2015, **54**, 12909–12913.

28 F. Ahmed, N. Tsujii and T. Mori, Thermoelectric properties of $CuGa_{1-x}Mn_xTe_2$: power factor enhancement by incorporation of magnetic ions, *J. Mater. Chem. A*, 2017, **5**, 7545.

29 Y. Zheng, T. Lu, M. M. H. Polash, M. Rasoulianboroujeni, N. Liu, M. E. Manley, Y. Deng, P. J. Sun, X. L. Chen, R. P. Hermann, D. Vashaee, J. P. Heremans and H. Zhao, Paramagnon drag in high thermoelectric figure of merit Li-doped MnTe, *Sci. Adv.*, 2019, **5**, eaat9461.

30 J.-B. Vaney, S. A. Yamini, H. Takaki, K. Kobayashi, N. Kobayashi and T. Mori, Magnetism-mediated thermoelectric performance of the Cr-doped bismuth telluride tetradymite, *Mater. Today Phys.*, 2019, **9**, 100090.

31 N. Tsujii, A. Nishide, J. Hayakawa and T. Mori, Observation of enhanced thermopower due to spin fluctuation in weak itinerant ferromagnet, *Sci. Adv.*, 2019, **5**, eaat5935.

32 S. Hébert, R. Daou, A. Maignan, S. Das, A. Banerjee, Y. Klein, C. Bourgès, N. Tsujii and T. Mori, Thermoelectric materials taking advantage of spin entropy: lessons from chalcogenides and oxides, *Sci. Technol. Adv. Mater.*, 2021, **22**, 583–596.

33 H. Chang, X. Gui, S. Huang, R. Nepal, R. Chapai, L. Xing, W. Xie and R. Jin, Mn-induced ferromagnetism and enhanced thermoelectric properties in $Ru_{1-x}Mn_xSb_{2+\delta}$, *New J. Phys.*, 2019, **21**, 033008.

34 S. Yousuf and D. C. Gupta, Investigation of electronic, magnetic and thermoelectric properties of Zr_2NiZ (Z = Al, Ga) ferromagnets, *Mater. Chem. Phys.*, 2017, **192**, 33–40.

35 J. Perdew, K. Burke and M. Ernzerhof, Generalized Gradient Approximation Made Simple, *Phys. Rev. Lett.*, 1996, **77**, 3865.

36 Y. Zhang and W. Yang, Comment on Generalized Gradient Approximation Made Simple, *Phys. Rev. Lett.*, 1998, **80**, 890.

37 F. Tran and P. Blaha, Accurate Band Gaps of Semiconductors and Insulators with a Semilocal Exchange-Correlation Potential, *Phys. Rev. Lett.*, 2009, **102**, 226401.

38 P. E. Blochl, O. Jepsen and O. K. Andersen, Improved tetrahedron method for brillouin-zone integrations, *Phys. Rev. B: Condens. Matter Mater. Phys.*, 1994, **49**, 16223–16233.

39 *An Augmented Plane Wave and Local Orbitals Program for Calculating Crystal Properties*, P. Blaha, K. Schwarz, G. K. Madsen, D. Kvasnicka, J. Luitz and K. Schwarz, WIEN2K, 2001.

40 G. K. H. Madsen, P. Blaha, K. Schwarz, E. Sjostedt and L. Nordstrom, Efficient linearization of the augmented plane-wave method, *Phys. Rev. B: Condens. Matter Mater. Phys.*, 2001, **64**, 195134.

41 A. Bolzan, C. Fong, B. J. Kennedy and C. J. Howard, Structural Studies of Rutile-Type Metal Dioxides, *Acta Crystallogr.*, 1997, **B53**, 373–380.

42 H. J. Monkhorst and J. D. Pack, Special points for Brillouin-zone integrations, *Phys. Rev. B: Solid State*, 1976, **13**, 5188–5192.

43 V. Dinh, K. Sato and H. Katayama-Yoshida, Dilute magnetic semiconductors based on wide bandgap SiO_2 with and without transition metal elements, *Solid State Commun.*, 2005, **136**, 1–5.

44 F. D. Murnaghan, The Compressibility of Media under Extreme Pressures, *Proc. Natl. Acad. Sci. U. S. A.*, 1944, **30**(9), 244–247.

45 M. Batzill and U. Diebold, The surface and materials science of tin oxide, *Prog. Surf. Sci.*, 2005, **79**, 47–154.

46 M. Maki-Jaskari and T. Rantala, Band structure and optical parameters of the SnO_2 (110) surface, *Phys. Rev. B: Condens. Matter Mater. Phys.*, 2001, **64**, 075407.

47 A. F. Lamrani, M. Belaiche, A. Benyoussef and A. El Kenz, Electronic structures and ferromagnetism of SnO_2 (rutile) doped with double-impurities: first-principles calculations, *J. Appl. Phys.*, 2014, **115**, 013910.

48 J. Themlin, R. Sporken, J. Darville, R. Caudano, J. Gilles and R. Johnson, Resonant-photoemission study of SnO_2 : cationic origin of the defect band-gap states, *Phys. Rev. B: Condens. Matter Mater. Phys.*, 1990, **42**, 11914.

49 H. Ehrenreich and H. Philipp, Optical Properties of Ag and Cu, *Phys. Rev.*, 1962, **128**, 1622.

50 F. Wooten, *Optical properties of Solids*, Academic Press, New York, 1972.

51 T. Serin, N. Serin, S. Karadeniz, H. Sari, N. Tuğluoğlu and O. Pakma, Electrical, structural and optical properties of SnO_2 thin films prepared by spray pyrolysis, *J. Non-Cryst. Solids*, 2006, **352**, 209–215.



52 P. Saikia, A. Borthakur and P. K. Saikia, Structural, optical and electrical properties of tin oxide thin film deposited by APCVD method, *Indian J. Phys.*, 2011, **85**(4), 551–5589.

53 L. Yanlu, F. Weiliu, S. Honggang, C. Xiufeng, L. Pan, Z. Xian, H. Jingcheng and J. Minhua, Optical Properties of the High-Pressure Phases of SnO_2 : First-Principles Calculation, *J. Phys. Chem. A*, 2010, **114**, 1052–1059.

54 E. Klampaftis, D. Ross, K. R. McIntosh and B. S. Richards, Enhancing the performance of solar cells *via* luminescent down-shifting of the incident spectrum: a review, *Sol. Energy Mater. Sol. Cells*, 2009, **93**, 1182–1194.

55 A. F. Lamrani, Rare-earth-doped TiO_2 rutile as a promising ferromagnetic alloy for visible light absorption in solar cells: first principle insights, *RSC Adv.*, 2020, **10**, 35505.

56 H. R. Mahida, D. Singh, Y. Sonvan, P. B. Thakor, R. Ahuja and S. K. Gupta, The influence of edge structure on the optoelectronic properties of Si_2BN quantum dot, *J. Appl. Phys.*, 2019, **126**, 233104.

57 G. K. H. Madsen, J. Carrete and M. J. Verstraete, BoltzTraP2, a program for interpolating band structures and calculating semi-classical transport coefficients, *Comput. Phys. Commun.*, 2018, **231**, 140–145.

58 B. Ryu and M. Oh, Computational Simulations of Thermoelectric Transport Properties, *J. Korean Ceram. Soc.*, 2016, **53**, 273–281.

59 G. K. H. Madsen and D. J. Singh, BoltzTraP. A code for calculating band-structure dependent quantities, *Comput. Phys. Commun.*, 2006, **175**, 67–71.

60 I. Ohkubo and T. Mori, Origin of Projected Excellent Thermoelectric Transport Properties in d^0 -Electron AMN_2 ($\text{A} = \text{Sr}$ or Ba ; $\text{M} = \text{Ti}$, Zr , Hf) Layered Complex Metal Nitrides, *Eur. J. Inorg. Chem.*, 2015, 3715–3722.

61 I. Ohkubo and T. Mori, Anisotropic Anomalies of Thermoelectric Transport Properties and Electronic Structures in Layered Complex Nitrides AMN_2 ($\text{A} = \text{Na}$, Cu ; $\text{M} = \text{Ta}$, Nb), *Chem. Mater.*, 2015, **27**(21), 7265–7275.

